ECAP-2019-018

Temperature dependent reverse bias IV-curve measurements of VUV-sensitive SiPMs

Bachelorarbeit aus der Physik

Vorgelegt von:

Constantin Rauch

13.12.2019

Erlangen Centre for Astroparticle Physics

Friedrich-Alexander-Universität Erlangen-Nürnberg

Betreuer: PD Dr. Thilo Michel

Contents

1 Introduction **1**

2 Theoretical background **3**
- 2.1 Neutrinoless double beta decay . . . 3
- 2.2 Detection of single photons . . . 3
- 2.3 Semiconductor detectors . . . 4
- 2.4 Avalanche photodiodes (APD) . . . 5
- 2.5 Silicon photomultiplier (SiPM) . . . 7
- 2.6 IV characteristics for reverse bias . . . 8

3 Experimental setup and measurement procedure **11**

4 Data analysis **15**
- 4.1 Breakdown voltage . . . 15
- 4.2 Dynamic range . . . 16

5 Results **19**
- 5.1 VUV3 . . . 19
- 5.2 VUV4 . . . 24
- 5.3 FBK LF2016 . . . 29

6 Summary and Conclusion **35**

7 References **37**

8 Appendix **39**

Acknowledgments **43**

Statutory Declaration **45**

1 Introduction

The nEXO experiment, which tries to find evidence for the neutrinoless double beta decay, requires photodetectors with high photon detection efficiency for Xenon scintillating light at 178 nm. Other experiments with liquid argon or experiments for the direct search for dark matter also require photodetectors capable of detecting photons in the VUV range [1], referring to photons with wavelengths shorter than 200 nm. One of the best suited detector types are silicon photomultiplier (SiPM). They offer excellent detection efficiency properties, single photon resolution, are mechanically robust and can be manufactured with matchless radiopurity in a shape that makes them easily scalable. Unlike photomultiplier tubes (PMT), they can be operated within magnetic fields and require low bias voltages smaller than 100 V. Their low space requirement and low power consumption allows for the usage of a large number of SiPMs in conjunction in a single experimental setup, thus creating large photosensitive areas. All this makes SiPMs excellent candidates for photodetectors in low background experiments.

All SiPMs used in the nEXO experiment will have to be completely characterized before they can be installed to sort out sensors with production faults and to properly investigate the photon collection efficiency. This process takes a very long time when using the currently available methods as described in [2]. A new method using only reverse current measurements for characterizing SiPMs is proposed in [3]. This method would accelerate characterization efforts tremendously.

Many of the properties of SiPMs are strongly dependent on the temperature at which the detector is operated, due to the fact that they are semiconductor devices. The nEXO experiment is planned to be conducted at about -100°C, therefore dependencies in this temperature regime are of special interest.

The following thesis aims to measure reverse bias IV-characteristics of different SiPM models at low temperatures. Special attention is paid to the dynamic range and the breakdown voltage, a crucial property for Geiger mode detectors such as SiPMs.

2 Theoretical background

2.1 Neutrinoless double beta decay

The goal for the nEXO experiment is the direct measurement of the proposed neutrinoless double beta decay in ^{136}Xe within a large liquid xenon volume [4]:

$$^{136}\mathrm{Xe} \rightarrow ^{136}\mathrm{Ba} + 2\mathrm{e}^{-} \tag{1}$$

It is necessary, that the neutrino is its own antiparticle for this process to occur, as to not violate lepton number conservation [5]. In the standard model of particle physics this is not the case.
A competing process, that is compatible with the standard model of physics is essentially two single beta decays happening simultaneously.

$$^{136}\mathrm{Xe} \rightarrow ^{136}\mathrm{Ba} + 2\mathrm{e}^{-} + 2\bar{\nu} \tag{2}$$

Momentum and energy can be distributed freely over the four products: Two electrons and two antineutrinos. The energy spectrum of detected electrons is therefore continuous with a maximum at the Q-value of the reaction, meaning the total mass difference between the initial and final particles and nuclei. For the neutrinoless double beta decay momentum and energy conservation demand that both ejected electrons must have the same energy. The energy spectrum for this process subsequently shows a monoenergetic peak at the Q-value [6, 4].
By measuring this peak, nEXO could proof the existence of the neutrinoless double beta decay. As the electrons enters the xenon, scintillating light is emitted. By detecting the scintillation photons, the energy of the original electron can be reconstructed [6]. The energy resolution needs to be excellent, since noise that is detected within the Q-value peak limits the sensitivity of the experiment [7].

2.2 Detection of single photons

Detecting single photons requires detectors with distinct properties. Firstly, a high photon detection efficiency ensures that an incident photon is detected with a high probability. Additionally, a high intrinsic amplification is needed in order to create a signal that can be read out by external electronics. Finally, the intrinsic noise within the detector must at least be equal but preferably lower than the signal resulting from one photon. To this day, one of the most reliable detectors capable of fulfilling the aforementioned requirements are photomultiplier, often in form of a photomultiplier tube (PMT). Photons create single electrons through the external photo effect within a photo cathode in these devices. The free electrons are accelerated with high voltages between several dynodes, where they create secondary electrons, and an exponential amplification of the signal is achieved. The resulting current can be measured as a voltage drop over a known resistor. While this design has proven to be functional in many applications, several major disadvantages make it unsuitable for special use cases. One of the biggest disadvantages is the PMTs sensitivity to magnetic fields, which divert electron trajectories, preventing them from reaching the dynodes. Other disadvantages include the necessity of high voltages and a high power consumption, combined with high complexity in construction resulting in mechanical fragility and often radioactive contamination. Radioimpurity introduces noise within the detector impeding measurement efforts of rare decays such as the neutrinoless double beta decay. Over the past decades, advancements in semiconductor technology facilitated new types of detectors capable of replacing the PMT [8, 9].

2.3 Semiconductor detectors

The most common material used for creating semiconductor photon detectors is silicon, the cheapest and best understood semiconductor. The conductivity of an ideal semiconductor is dominated by the amount of free charge carriers within the material. This amount is determined by the available states in the conduction band, the band gap between the valence and the conduction band and the temperature of the semiconductor. Electrons may change their state from one band into a free state within the other band, provided momentum and energy is conserved for this transition. This can be achieved by exchanging momentum and energy with the lattice or by absorbing incident photons. When an electron within the valence band is excited into the conduction band, an empty state, a so called “hole”, is left vacent. This vacancy can be filled by other electrons and is not localized within the lattice, essentially forming a freely moving positive charge carrier.

Electrical properties like the conductivity can be easily manipulated by doping the semiconductor with atom types not usually present within the lattice. If atoms with five valence electrons such as phosphorus are added into the silicon lattice, additional electrons are provided. If atoms with three atoms are added, additional holes are provided. These additional states lie within the band gap between valence and conduction band and require far less energy to be excited. A semiconductor is called “n-doped” if it has predominately negative charge carriers and it is called “p-doped” if mainly holes contribute to its conductivity. The dominating carrier type is called “majority carrier”.

One of the main mechanisms for photon detection in semiconductors is the internal photo effect: A single or multiple electrons are excited into the conduction band of the semiconductor by incident photons. The excited electron may have its origin within the valence band or the states provided by doping. The conductivity of the semiconductor changes with the luminosity of incident light, as long as each photon has enough energy to excite an electron. This requires the energy of the bandgap in the case of an excitement from the valence band [8].

Free charge carriers are also produced by thermal excitement of electrons. The required excitation energy in this case is provided by the lattice. When a signal is read out, the origin of its charge carriers can no longer be distinguished. Thermally created charge carriers will always produce a certain noise level, but the amount of carriers created in this way is strongly dependent on the temperature at which the detector is operated. Thermal noise can be reduced significantly by cooling the device [9].

2.4 Avalanche photodiodes (APD)

Avalanche photo diodes consist at least of a p-n junction, meaning that a p-doped volume is implanted into a mainly n-doped crystal. The n-doped region provides additional electrons, which move along the concentration gradient into the p-doped region, where they get trapped in the states provided by the doping atoms. This creates a depletion zone, where the total number of free charge carriers drops significantly compared to an intrinsic non-doped crystal [13, p. 11]. An effective charge density is formed in the vicinity of the junction as more and more negatively charged electrons move into the previously neutral p-region and vice versa. This results in an electric field to be established until a state of dynamic equilibrium is reached such that the concentration gradient and the coulomb force compensate each other. The electric field additionally prevents majority charges from passing the junction. As a result the conductivity of the p-n junction is reduced to almost zero, effectively creating an insulator.

The volume of the depletion zone can be expanded by applying negative voltage to the p-doped region and positive voltage to the n-doped region. Charge carriers are pulled towards their terminal and away from the depletion zone by this so called “reverse bias voltage”. This reduces the number of free charge carriers further. The volume of the depletion zone can also be increased by inserting a layer of non-doped silicon into the p-doped region. This doping structure is called “pipn-diode” and it is depicted in Figure 1. The “+” next to p and n indicates an especially high doping density. Free charge carriers within the intrinsic layer are removed by the external voltage,

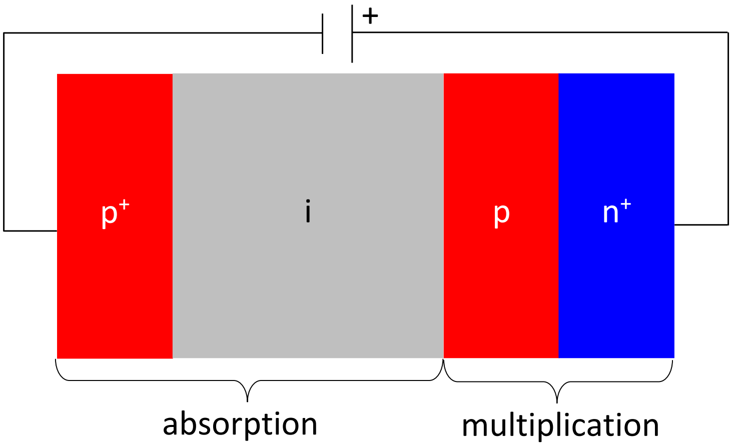

Figure 1: Doping structure of a pipn-APD.

creating a large volume sensitive to photons. The charge multiplication is still happening close to the p-n-junction, meaning that free charge carriers need to drift from the absorption zone to the multiplication zone [9].

Avalanche photo diodes are photo diodes with intrinsic amplification of flowing current. This amplification is achieved by increasing the applied reverse bias voltage close to the breakdown voltage at which the junction becomes conductive. The applied reverse bias voltage not only makes sure that the sensitive volume is depleted of charge carriers, but also accelerates free charge carriers within the avalanche or multiplication zone surrounding the junction (Figure 1). The avalanche zone is usually significantly smaller than the volume in which photons are absorbed. Due to the high electric fields within the avalanche zone, charge carriers gain a large amount of kinetic energy, which can be used to create new free electron-hole pairs via impact ionization. These are also accelerated and can themselves create further free charge carriers. This so called avalanche breakdown achieves an exponential charge multiplication depending mainly on the applied bias voltage. The higher the voltage, the higher the gain. This enables the detection of a small number of coinciding photons with an APD. [9].

Reverse bias voltage can also be increased to levels above breakdown voltage. A single free charge carrier within the depletion zone has the potential to trigger a breakdown if such a high voltage is applied. The current must be stopped by adding additional devices to the circuit, as the voltage above breakdown means, that the junction remains conductive once current flows. Every breakdown therefore leads to a short current pulse. This mode of operation is often called Geiger mode, as it resembles the working principle of a Geiger counter.

2.5 Silicon photomultiplier (SiPM)

Silicon photomulitplier are built by connecting multiple APDs together in parallel, arranging them in an array and operating them in Geiger mode. A SiPM and its equivalent electrical circuit is depicted in Figure 2. The applied voltage is increased to values larger than breakdown voltage of the individual microcells in order to increase gain and photon detection efficiency significantly. A quenching resistor is added in series to each diode to prevent self destruction when a breakdown is triggered. One of the main advantages of SiPM compared to PMTs is, that all the necessary structures can be created by well established processes for producing microchips [9, 11].

As soon as current flows through the diode and subsequently the corresponding quenching resistor, the voltage drop over the resistor rises and pulls down the bias voltage over the diode to below breakdown voltage, ending the breakdown avalanche. Once the flow of current is stopped, the depletion zone within the semiconductor has to be reestablished. During this time the detector can not output a signal of full amplitude.

A full discharge can be triggered by a single free charge, meaning that the detector is able to detect single photons. In reality this is limited by a number of factors: Some incident photons are reflected out of the detector without

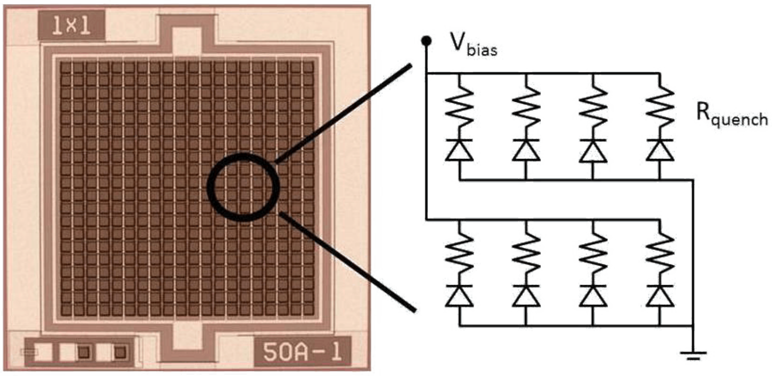

Figure 2: Silicon photomultiplier on the left and equivalent electrical circuit on the right. The small rectangular structures are the individual microcells consisting of an APDs and a quenching resistor [15]

.

creating a free charge carrier. The incident light might hit an insensitive part of the surface of the detector. A photon within the detector might not create free charge carriers, but deposit its energy differently. Finally, a free charge carrier within the depletion region has a certain probability not to trigger an avalanche or drift away from the avalanche zone.

The probability for triggering avalanches is generally different for electrons and holes [14]. Electrons will only trigger an avalanche if they are created within the p-region, and, vice versa, holes can only be detected when they are within the n-doped region. As VUV light is absorbed in the topmost layers, almost all free charges contributing to the signal are electrons [3]. Thermally generated charge carriers are created independent from the location. The n-region typically has a much larger volume in SiPMs optimized for VUV detection, meaning that dark current is dominated by avalanches triggered by holes [3]. This dark current is not distinguishable from current caused by incident light. As a result, a certain amount of photons is needed in order for the signal to rise above noise levels. Differences in avalanche triggering probabilities for electrons and holes can be used to gain information about the structure and main characteristics of the detector [14, 3].

Once current flows through a microcell of a SiPM, different processes may cause unwanted distortion of the signal. Some charge carriers within a breakdown avalanche can get trapped within states created by lattice impurities. They are usually released shortly after but a second avalanche discharge may be triggered. This process is called “afterpulsing”. Another common process is “crosstalk”. During an avalanche discharge photons are created within a SiPM cell. These photons can travel to neighboring cells and trigger an avalanche discharge. Both processes add to the integrated current through the cell [9].

The signal ultimately measured is composed of all the currents of the individual cells. The strongest detectable signal is reached when all cells are triggered simultaneously with a frequency equal to the inverse time required to recharge the cells, but saturation effects begin to show earlier [8].

2.6 IV characteristics for reverse bias

This thesis examines the properties of SiPM when reverse bias voltage is applied. Properties for a SiPM are generally those of a standard diode operated with reverse voltage as plotted in Figure 3, since they are mainly composed of a large number of diodes.

Only a small current, the so called reverse leakage current, passes through the detector for low voltages. This current is caused by minority charge carriers in the depletion zone that can pass the p-n-junction as their charge

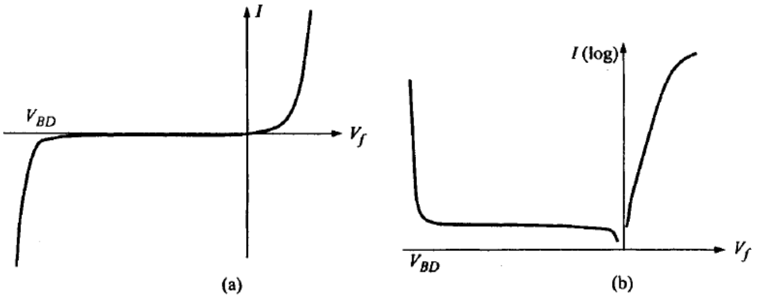

Figure 3: Diode characteristics plotted with a linear (a) and logarithmic (b) y-scale. Depicted are forward bias for voltages larger zero and reverse bias for voltages smaller than zero [13, p. 15].

allows them to pass the field gradient. Electrons act as minority charges within the p-region, while holes fulfill the same role in the n-region. Free minority charges are created in the same ways as majority charges, therefore the reverse leakage current increases with temperature because the number of free charge carriers increases with increasing thermal energy. The applied voltage is too small to create avalanche discharges, no charge multiplication takes place, limiting the flowing current.

At a certain voltage V_{BD}, the so called breakdown voltage, the current increases drastically, the detector becomes conductive. The applied voltage is large enough for avalanches to be triggered by free charge carriers within each cell. The repeated avalanche discharge can be measured as a continuous current at the terminals of the SiPM. The current will increase very strongly [10], as more and more charge carriers can trigger breakdown avalanches for a small voltage interval following the breakdown. The increase of current at breakdown voltage can be approximated by [12]:

$$I = c' \cdot (V - V_{\mathrm{BD}})^n \tag{3}$$

The inverse derivative of the logarithm of I has therefore the following form:

$$\left(\frac{\mathrm{d}\log(I)}{\mathrm{d}V}\right)^{-1} = c \cdot (V - V_{BD}) \tag{4}$$

where log denotes the natural logarithm. The breakdown voltage is, like the reverse leakage current, dependent on the temperature [9].

By further increasing the applied voltage, the avalanches become self sustaining. At this point the voltage drop over the quenching resistor is no longer sufficient to pull the diode below breakdown voltage. Breakdown avalanches are triggered permanently and if too much heat is generated, the detector will be destroyed [8].

3 Experimental setup and measurement procedure

In this thesis reverse bias voltage measurements for three different SiPM models are taken. These detectors are two detectors from the S 13370/S13371 MPPC series by Hamamatsu photonics, named in the following VUV3 and VUV4, and LF2016 produced by FBK. IV-curves are taken by supplying a voltage to the detector and simultaneously measuring flowing currents with a picoammeter. Hamamatsu SiPMs start to break down at voltages around 55 V. An ISEG SHQ122M high voltage power supply, allowing voltages up to 2 kV with a granularity of 0.1 V [16] is used to surpass this voltage. The current is measured by a Keithley 6485 picoammeter. Its internal RMS noise level of $2 \cdot 10^{-14}$ A [17] provides the precission required to measure reverse leakage currents while its range of up to to 20 mA makes it also suitable for measuring the significantly higher currents above breakdown voltage. Electrical connections are achieved by LEMO coaxial cables. A specifically designed box allows for the splitting of a coaxial cable into two single cables to achieve current measurements. The entire measurement setup is sketched in Figure 4.

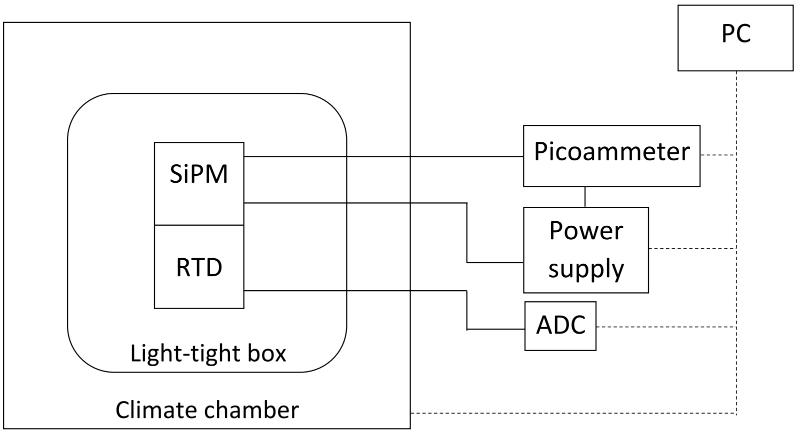

Figure 4: Sketch of the measurement setup. Device designations can be found in the text.

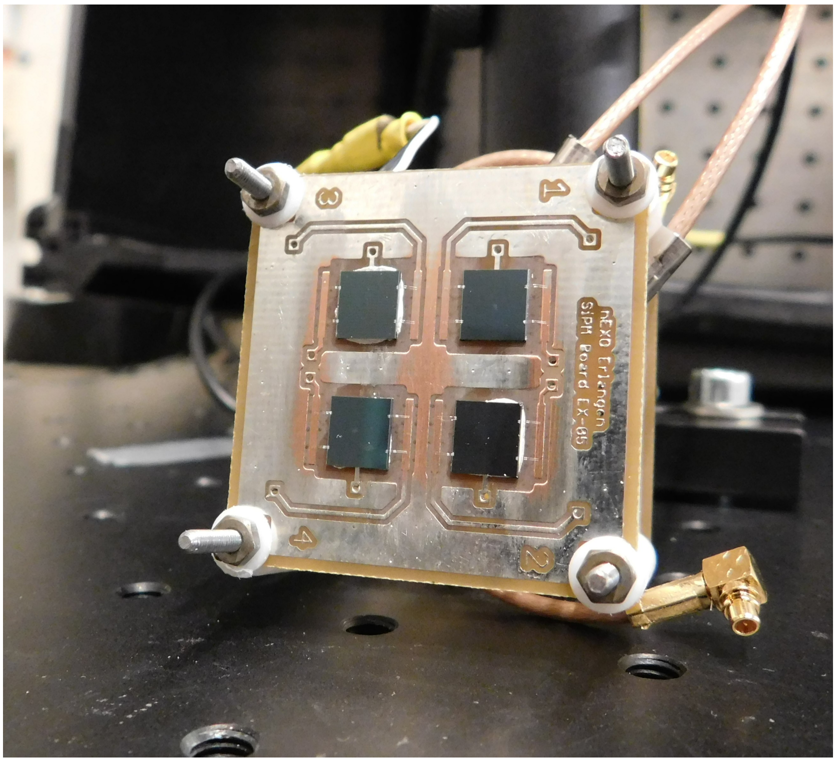

Figure 5: FBK LF2016 on measurement fixture. The temperature sensor is mounted on the backside of the PCB.

The SiPMs are connected directly to the picoammeter and power supply as a preamplifier would alter electrical characteristics. Current measurements therefore need to be performed at currents down to 10^{-12} A, necessitating the use of a picoammeter. Previous tests had shown that a FLUKE DMM did not provide the low noise levels to perform the planned measurements.
A HEL-705 RTD 100 Ω platinum film sensor from the Honywell RTD series [18] is also attached to the SiPM board, in order to monitor and record temperatures. It is read out by a Meilhaus electronic RedLab 3104 ADC/DAC [19] via four wire resistance measurement. After a calibration of the ADC with the program instaCal, TracerDAQ is used to record temperature measurements.
The board with the SiPM and temperature sensor is placed on an optical table, an image of the board can be found in Figure 5. A box is placed over the detector in order to prevent any light from hitting the detector as all measurements are to be carried out as dark measurements. The box is sealed on all sides with duct-tape, closing all joints as light-tight as possible. The measurement leads can be connected to devices outside the box through

two small holes on the side of the box. The optical table and the lid are made of metal, providing additional thermal mass. This helps in stabilizing the temperature of the detector during measurements.

A Testequity 1007C temperature chamber is used, in order to take measurements at different temperatures. It supports temperatures down to −70°C, at a rated typical stability of ±0.2 °C [20]. The light tight box is placed inside the climate chamber. For additional light insulation the front window of the 1007C is sealed using duct tape and a black cloth is placed over the front door, covering the joints and also the isolated cable feedthrough at the side of the climate chamber.

All devices necessary for measurement can be controlled by a computer running python scripts. A python script controlls the applied voltage and triggers measurements. A 2 s break is programmed to provide enough time for the voltage to stabilize, after each voltage is set. The actual applied voltage is then read out and saved to a textfile. Next, a current measurement is performed and the returned current is also saved. The picoammeter is set to auto range and averages over ten power line cycles (NPLC 10). The current measurement could be repeated any number of times to improve measurement statistics. Once all current measurements are completed, the script increases the bias voltage by a set amount and repeats the measurements. The process stops once a fixed end voltage is reached or at any time when the current is observed to exceed a certain limit.

Measurements are taken at ten temperatures from +20 °C to -70 °C for the Hamamatsu VUV3 and nine temperatures each for Hamamatsu VUV4 and FBK LF2016 from +10 °C to -70 °C. As measured noise increases noticeably when the climate chamber is running during measurements, the climate chamber is switched off before measurements are taken. The temperature stays constant within the climate chamber for about 15 minutes so measurements need to be finished in a short amount of time. Measurements with one current readout per voltage step and a step size of 0.2 V complete within the available time frame. The short measurement duration has the additional benefit of reducing internal warm up of the detector under test due to the flowing current. An additional histogram is taken for each temperature step in order to estimate statistical uncertainties. Current is measured 400 times without any applied voltage. This is conducted once with the ISEG power supply connected and once with only the SiPM plugged into the picoammeter. After all measurements are completed, the setpoint temperature of the climate chamber is lowered by 10 K. The next measurement is started, when the measured temperature of the platinum sensor does not deviate by more than 0.1 K for the typical duration of one measurement. The temperature chamber cools for at least 2 h before this equilibrium is reached.

4 Data analysis

4.1 Breakdown voltage

The breakdown voltage can be determined by using Equation 4. First, the inverse derivative of the logarithm of measured currents is calculated by using the python module numpy. A linear fit is then performed to these values with the scipy module curve_fit, which uses the least squares method.
The current measurements are subject to statistical measurement errors. These errors are estimated by using the histograms measured at each temperature. After applying error propagation to each of the standard deviations obtained from the histograms, the errors are used as uncertainties on the measured I-values from the IV-measurements. The error propagation for each part of $(\mathrm{d}\log(I)/\mathrm{d}V)^{-1}$ can be calculated as follows:

$$\Delta(\log(I)) = \left|\frac{\mathrm{d}\log(x)}{\mathrm{d}x}\right| \Delta x = \left|\frac{\Delta x}{x}\right| \tag{5}$$

$$\Delta(1/x) = \left|\frac{\mathrm{d}}{\mathrm{d}x}\left(\frac{1}{x}\right)\right| \Delta x = \left|\frac{\Delta x}{x^2}\right| \tag{6}$$

The propagation of the error when differentiating is estimated by using the numerical definition:

$$\Delta\left(\frac{\mathrm{d}x}{\mathrm{d}y}\right) \approx \Delta\left(\frac{(x_2 + \Delta x_2) - (x_1 + \Delta x_1)}{\delta y}\right) = \Delta\left(\frac{x_2 - x_1 + (\Delta x_2 - \Delta x_1)}{\delta y}\right) \tag{7}$$

Here x_1, x_2 are deterministic quantities, $\Delta x_1, \Delta x_2$ are stochastic variables representing the measurement error and δy is the step size in between two measurements. $\Delta x_1, \Delta x_2$ are both drawn from the same probability distribution. For an estimation a Gaussian distribution with standard deviation σ is assumed for Δx. The combined variable

$$z := \Delta x_2 - \Delta x_1 \tag{8}$$

is also a random variable. Its distribution is obtained via convolution:

$$N(z, 0, \Delta z) = N(-\Delta x_1, 0, \sigma) \star N(\Delta x_2, 0, \sigma) = \int_{\infty}^{\infty} N(-x, 0, \sigma) N(z + x, 0, \sigma) dx \tag{9}$$

The result for z is:

$$N(z, 0, \Delta z) = \frac{1}{\sqrt{2\pi}} \frac{1}{\sqrt{2\sigma^2}} e^{\frac{z^2}{2\sigma^2}} \tag{10}$$

Therefore the sum is also Gaussian distributed and its error is

$$\Delta z = \Delta(\Delta x_2 - \Delta x_1) = \sqrt{2}\Delta x \tag{11}$$

This yields for the derivative:

$$\Delta\left(\frac{\mathrm{d}x}{\mathrm{d}y}\right) \approx \frac{\sqrt{2}}{\Delta y}\Delta x \tag{12}$$

Combining Equation 5, Equation 6 and Equation 12 the error for each data point of the IV-measurement can be estimated by:

$$\Delta\left(\frac{\mathrm{d}\log(I)}{\mathrm{d}V}\right)^{-1} = \frac{1}{\left(\mathrm{d}\log(I)/\mathrm{d}V\right)^2}\frac{\sqrt{2}\Delta I}{I\delta V} \tag{13}$$

where V is the applied voltage, ΔV the step size between voltages, I the measured current and ΔI the error on current measurement obtained from the respective histogram.

Scipy's curve_fit returns the optimal parameter for V_{BD} and an estimated covariance-matrix. The diagonal elements of the covariance-matrix contain estimated values for the variance of the fit parameters, which can be interpreted as squared fit uncertainties.

With breakdown voltages and uncertainties determined for all temperatures, a linear function

$$f(T) = m \cdot T + t \tag{14}$$

is fitted to the data set of V_{BD} over T. The fit uncertainties for V_{BD} are used as y-errors for the new fit.

By calculating the residuals, a goodness of fit test is performed for the fit. Reduced χ^2 is defined as:

$$\chi^2_{\text{reduced}} = \frac{1}{\text{n-2}}\sum_{i=1}^{n}\left(\frac{f(T_i) - V_{\mathrm{BD}}(T_i)}{\Delta V_{\mathrm{BD}}, i}\right)^2 \tag{15}$$

where n is the number of data points and $n-2$ is the number of degrees of freedom. For a fit to data points with Gaussian distributed errors, χ^2_{reduced} is expected to have a value of 1. The deviation of a fit from this value provides at least a statistical measure of how suitable the applied model and the estimated errors are.

4.2 Dynamic range

The current through the SiPM rises strongly at breakdown voltage as well as when self sustaining avalanches start to occur. As the current change is low before and after the breakdown occurs, a peak can be expected in the differentiated logarithmic IV-curve at the breakdown voltage. For sufficiently low temperatures, the IV-curve has a similar kink after the self sustaining avalanches set in. As a result, when plotting the derivative of $\log(I)$ over V one expects to see two distinct peaks. The space between those peaks can be defined as dynamic range where the detector can be safely operated: The amplification below breakdown voltage is not sufficient for detecting single photons, and as soon as self sustaining avalanches set in, large currents flow through the microcells, increasing noise and possibly damaging the detector. In order to determine the width of the dynamic range, the V values at half-height are read from the plots on the falling edge of the breakdown peak and on the rising edge of the self sustaining avalanche peak.

5 Results

5.1 VUV3

The first SiPM to be examined is the Hamamatsu VUV3 MPPC. Ten IV-curves with reverse bias voltage were measured at temperatures between +20°C and -70°C with a temperature step of 10 K. The obtained data sets are plotted in Figure 7 with the y axis scaled logarithmically. As expected, the reverse leakage current decreases with falling temperature due to the lower chance of free charge carriers being created by thermal energy. The reverse leakage current does not drop any further for temperatures below -10 °C, but the variance of measured currents increases. This is caused by noise introduced with the power supply. Connecting it to the circuit creates currents in the same order of magnitude or larger than the expected leakage current at lower temperatures, making measurements impossible. This can be seen in Figure 6. The histogram average and variance taken with only the SiPM connected is one order of magnitude smaller compared to the one taken with the ISEG power supply connected.

Breakdown voltage All data sets contain at least some part of the current increase for voltages larger than breakdown voltage, therefore the method described in subsection 4.1 can be used to determine the breakdown voltage. One example fit is shown in Figure 8. The procedure from subsection 4.1 was applied for all temperatures with the exception of -70 °C. At this temperature almost all of the data points were below the noise level causing problems for the numerical derivation. The results for all remaining temperatures are plotted in Figure 9. The breakdown voltage falls linear with temperature. Using the uncertainties obtained as described in subsection 4.1, a linear model was fitted to the data in order to extrapolate the breakdown voltage for a wider range of temperatures. The following relation was found:

$$V_{\mathrm{BD}} = (0.0604 \pm 0.0016)\,\frac{\mathrm{V}}{^{\circ}\mathrm{C}} \cdot T + (50.675 \pm 0.023)\,\mathrm{V} \tag{16}$$

This yields for a target temperature of -100 °C, at which xenon is liquid, a breakdown voltage of:

$$V_{\mathrm{BD}}(-100\,^{\circ}\mathrm{C}) = (44.63 \pm 0.17)\,\mathrm{V} \tag{17}$$

The final fit residuals were also computed in order to evaluate the goodness of the fit. For the VUV3 detector

$$\chi^2_{\mathrm{reduced}} \approx 1.4 \tag{18}$$

as defined in Equation 15 was found. This value is very close to 1 supporting the choice of a linear model statistically.

Dynamic range From the IV measurements one can also determine the dynamic range of the detector, as described in subsection 4.2. To do so, the derivative of the logarithm of each IV measurement is plotted over the voltage. One example can be seen in Figure 11, the other temperatures are plotted in Figure 24. For temperatures below 0 °C, two distinct peaks can be seen: One at the beginning of the range and one at its end. The first peak corresponds to the breakdown voltage when the sudden rise in current creates a peak in the differentiated plot. The second peak occurs when so called self sustaining avalanches occur. The applied voltage at this point is so high, that the quenching resistors can no longer stop the avalanche breakdown. As a result, the current rises strongly once more. At temperatures below 10 °C a kink is visible in Figure 7 at a voltage of around 62.5 V. The following plateau has a small slope in the logarithmic plot, corresponding to a small derivative. This forms the falling edge of the second peak. At higher temperatures the region of self sustaining avalanches is reached directly after the breakdown occurs. This prohibits the formation of the second peak in the differentiated plot. As can be seen in Figure 11, the dynamic range is constant at about 11.8 V over most of the measured temperature range. Uncertainties are estimated by the achievable accuracy when reading values from a plot. The dynamic range at -10 °C is problematic, as no plateau is visible in Figure 7 at this temperature and therefore the peak in Figure 11 may be a numerical artifact.

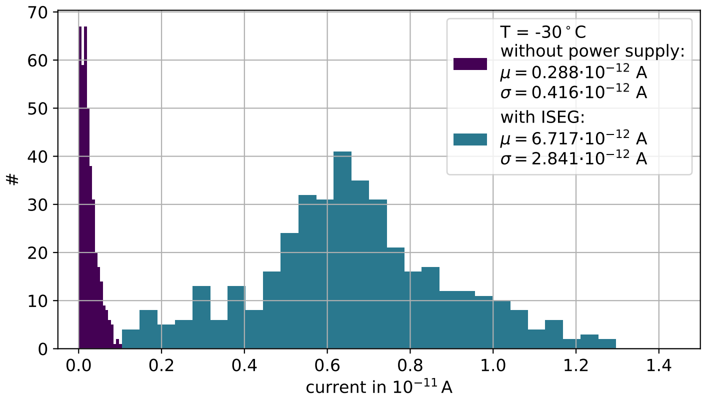

Figure 6: Histograms taken with VUV3. μ and σ denote the arithmetic mean and the standard deviation of the sample.

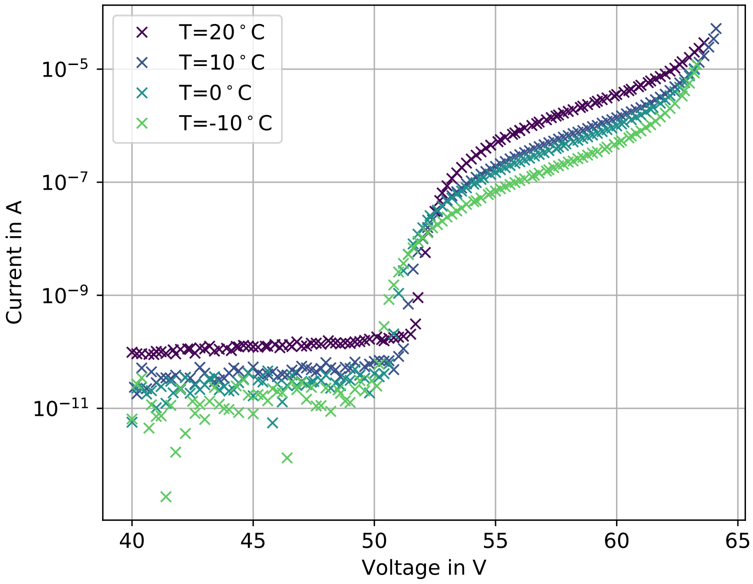

(a) IV-curves for temperatures from 20 °C to -10 °C.

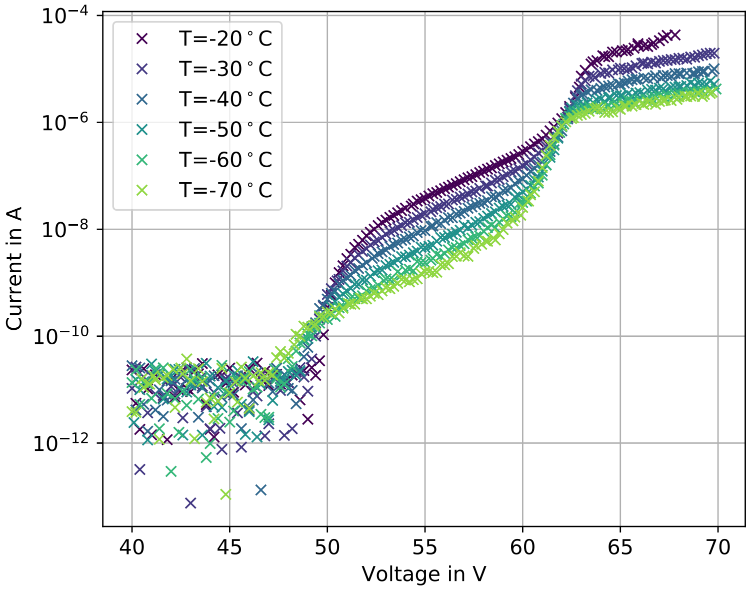

(b) IV-curves for temperatures from -20 °C to -70 °C.

Figure 7: IV-Characteristics for reverse bias of Hamamatsu VUV3.

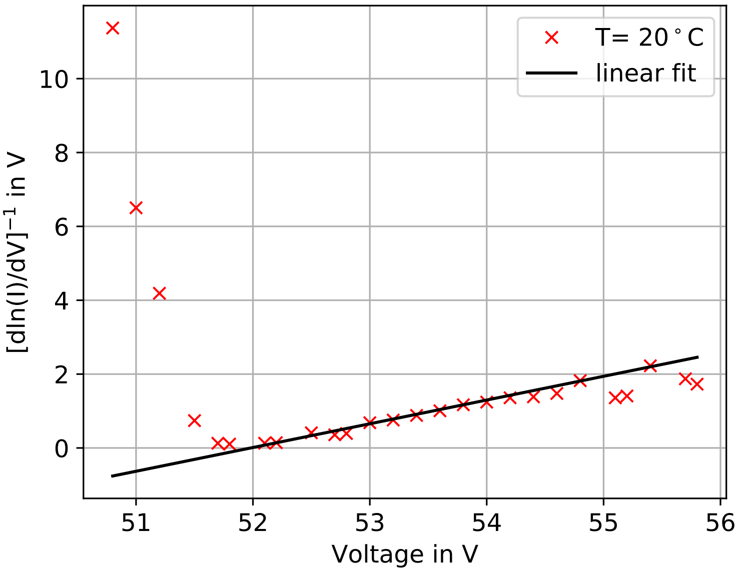

Figure 8: Example fit for determining the breakdown voltage of VUV3 at 20 °C.

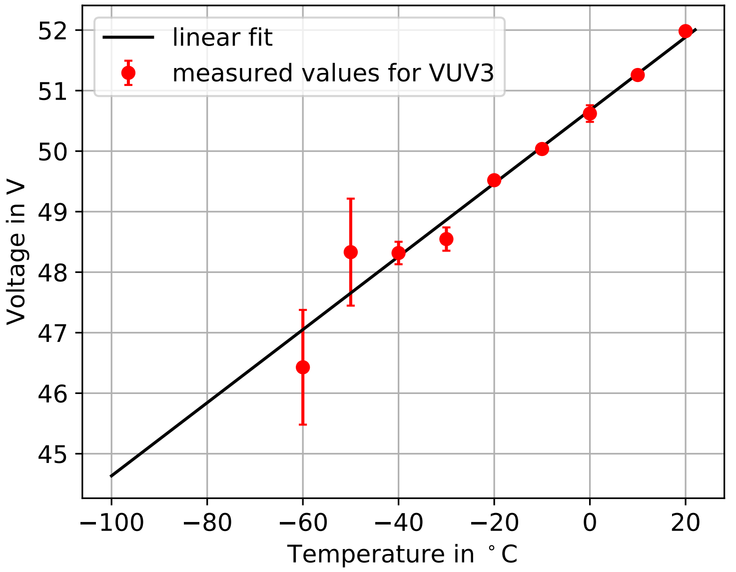

Figure 9: Plot of breakdown voltages for VUV3 with linear fit for extrapolation.

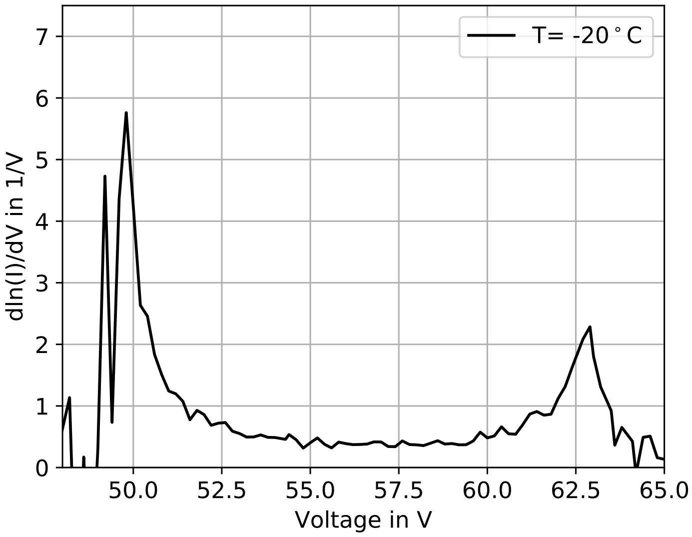

Figure 10: Derivative of the logarithmic current at -20 °C for VUV3.

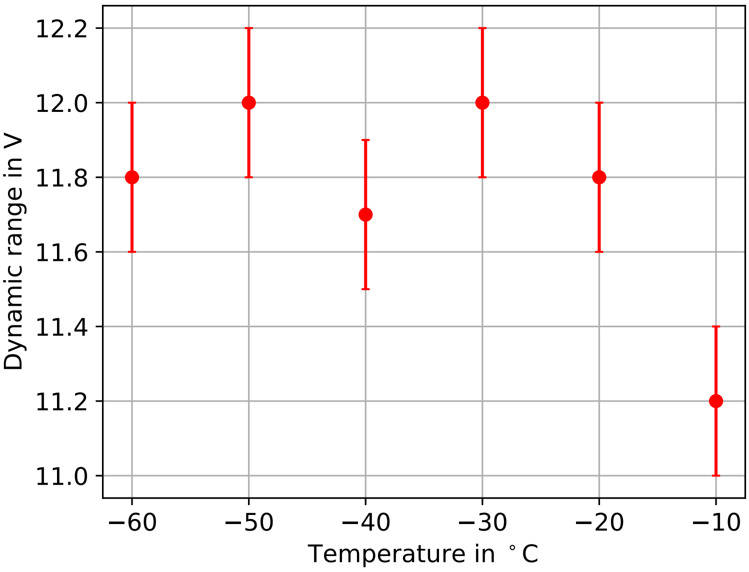

Figure 11: All dynamic ranges plotted together over their respective temperatures for VUV3.

5.2 VUV4

Hamamatsu's VUV4 is an updated version of the previously examined VUV3. IV measurements were taken for nine equidistant temperatures from +10 °C to -70 °C. The data sets are plotted in Figure 13. Compared to the VUV3 detector, the reverse leakage current is one order of magnitude smaller, but rises by approximately an order of magnitude per 20 K as well. Therefore noise starts to dominate the measurement of reverse leakage current in this detector only for temperatures below -20 °C. As before, the spread and average current seen in the histograms with the ISEG power is several orders of magnitude larger than without the power supply (Figure 12).

Breakdown voltage Breakdown voltage was determined once again by the method described in subsection 4.1 for every temperature step. One example fit is plotted in Figure 14, and a combined plot with all breakdown voltages is shown in Figure 15. A linear fit was performed in order to extrapolate the breakdown voltages for lower temperatures and the following parameters were obtained:

$$V_{\mathrm{BD}}(T) = (0.047 \pm 0.003)\,\frac{\mathrm{V}}{{}^\circ\mathrm{C}} + (50.19 \pm 0.07)\,\mathrm{V} \tag{19}$$

This amounts to a breakdown voltage of

$$V_{\mathrm{BD}}(-100\,^\circ\mathrm{C}) = (45.5 \pm 0.3)\,\mathrm{V} \tag{20}$$

at -100 °C, the temperature of liquid xenon. The breakdown voltage of VUV4 is only 1.6 V lower than the one of VUV3, showing an overall similarity of electrical characteristics between those two detectors. By using a different method for determining V_{BD}, [21] found a value of

$$V_{\mathrm{BD}} = 45.4 \tag{21}$$

which agrees within the margins of errors with the breakdown voltage found in this thesis.
A goodness of fit test was performed for the linear fit as it is described in subsection 4.1. The following was found:

$$\chi^2_{\mathrm{reduced}} \approx 1.0 \tag{22}$$

$\chi^2_{\mathrm{reduced}}$ equals the optimal value of 1, which once again supports the choice of a linear model for the temperature dependence of breakthrough voltages.

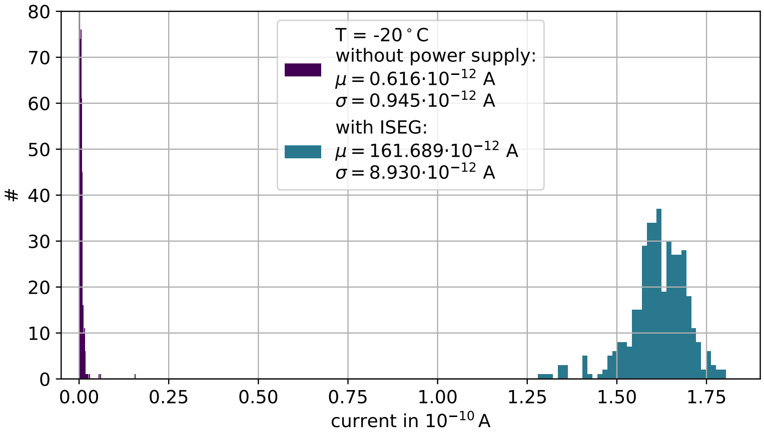

Figure 12: Histograms taken with VUV4. μ and σ denote the arithmetic mean and the standard deviation of the sample. Only a small peak is visible for the histogram obtained without the power supply.

Dynamic range The IV measurements were also used to determine the dynamic ranges for VUV4 at different temperatures as stated in subsection 4.2. Figure 16 and Figure 25 show the plots for all dynamic ranges of VUV4. The peak caused by self sustaining avalanches starts appearing below -10 °C. For all temperatures with two distinct peaks the dynamic range was determined. They are plotted together in Figure 17. The errors are estimated based on reading accuracy when determining voltages from a plot. The dynamic range is constant for VUV4 at around 9 V for the observed temperature range. It is about 3 V lower than that of VUV3. The falling edge of the self sustaining avalanche peak is not clearly visible in the plots for 0 °C and -10 °C and dynamic ranges may be subject to larger errors for these temperatures.

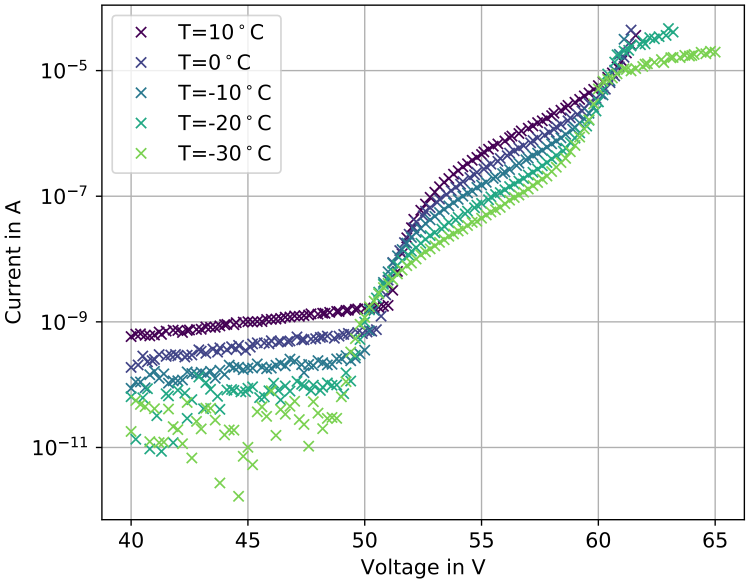

(a) Temperatures from 10 °C to -30 °C.

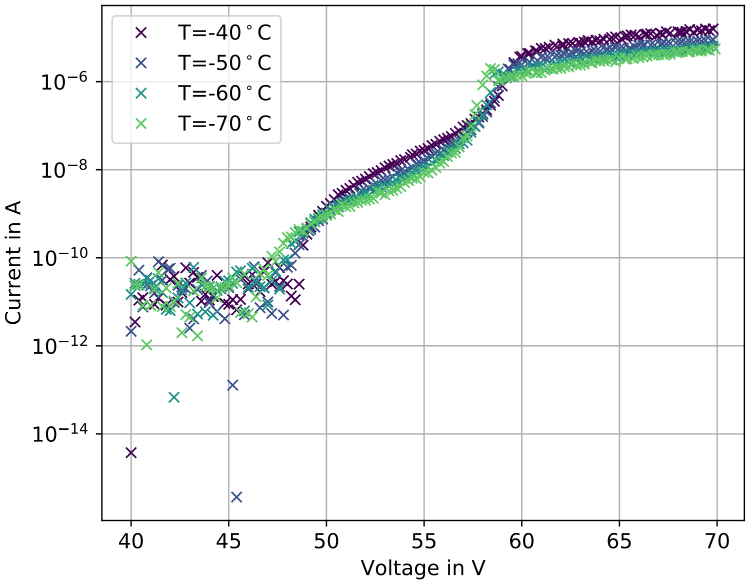

(b) Temperatures from -40 °C to -70 °C.

Figure 13: IV-Characteristics with reverse bias for Hamamatsu VUV4.

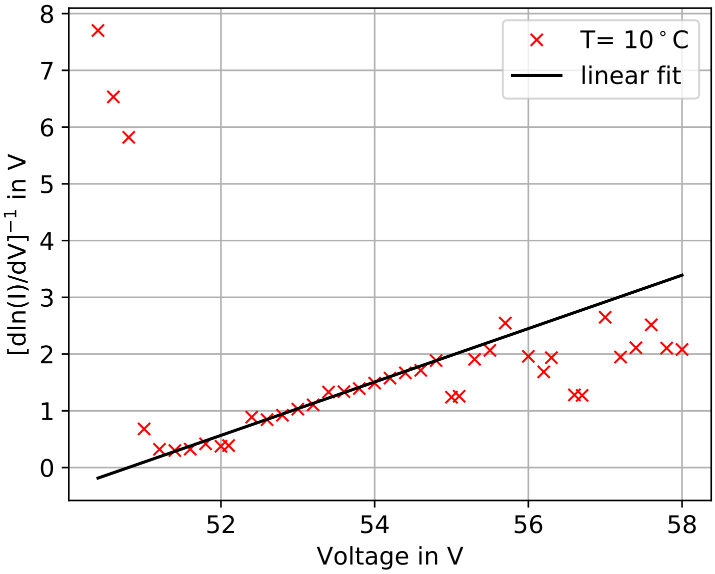

Figure 14: Example fit for determining the breakdown voltage of VUV4 at 10 °C.

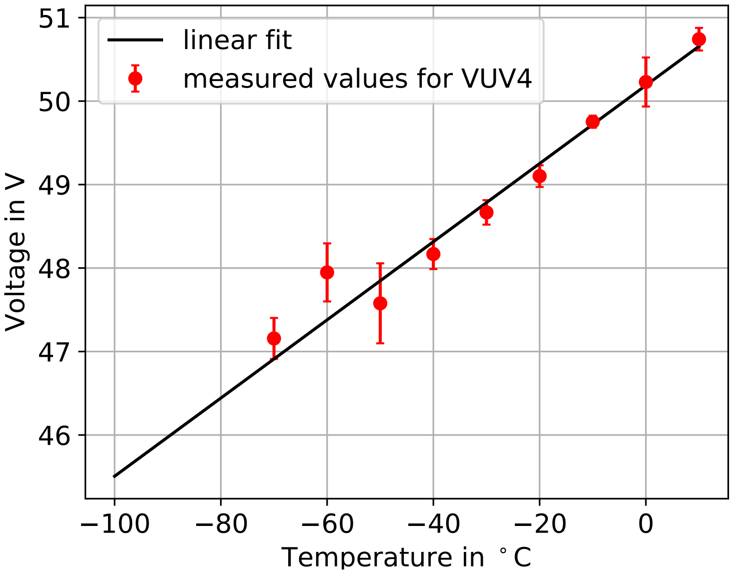

Figure 15: Plot of breakdown voltages for VUV4 with linear fit for extrapolation.

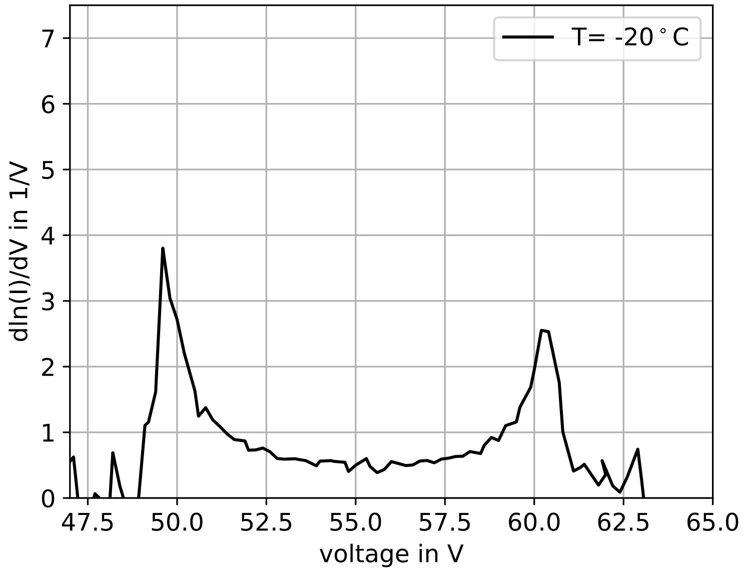

Figure 16: Derivative of the logarithmic current at -20 °C for VUV4.

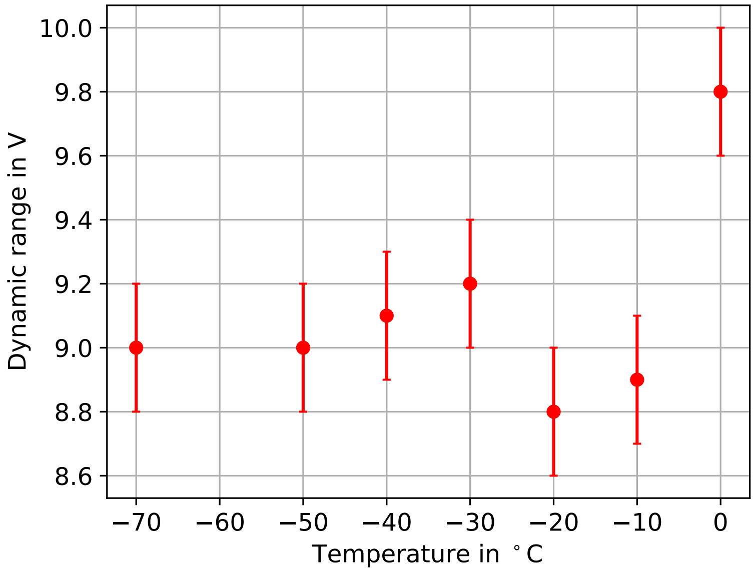

Figure 17: All dynamic ranges plotted together over their respective temperatures for VUV4.

5.3 FBK LF2016

The last SiPM to be examined in this thesis is the FBK LF2016, in the following denoted only as FBK. IV characteristics were taken for temperatures from 10 °C to -70 °C. The IV curves are shown in Figure 19. Compared to both Hamamatsu devices, the reverse leakage current is approximately an order of magnitude larger and the breakdown voltage is roughly 16 V lower. This may indicate a larger amount of impurities in the silicon lattice used in making FBK devices, since impurities act similar to doping atoms by providing states that are easily excited. Due to the overall higher leakage current, noise starts to influence the current measurement significantly not until temperatures below -20 °C. The variance and mean of currents obtained with the histogram measurements are significantly higher if the ISEG power supply is connected to the picoammeter. This can be seen in Figure 18, where two example histograms are plotted.

Breakdown voltage The procedure described in subsection 4.1 was performed with the obtained data. An example fit for the determination of $\mathrm{V}_{\mathrm{Breakdown}}$ at one temperature can be found in Figure 20. The results for all temperatures are shown in Figure 21. A linear fit was attempted in order to extrapolate the breakdown voltage to lower temperatures. The following values were obtained:

$$V_{\mathrm{BD}}(T) = (0.036 \pm 0.001)\,\frac{\mathrm{V}}{{}^{\circ}\mathrm{C}} \cdot T + (32.725 \pm 0.022)\,\mathrm{V} \tag{23}$$

For -100 °C this results in

$$V_{\mathrm{BD}}(-100\,{}^{\circ}\mathrm{C}) = (28.85 \pm 0.19)\,\mathrm{V} \tag{24}$$

The FBK has a noticeably lower breakdown voltage than both Hamamatsu detectors, but it also varies less with temperature. Compared with the breakdown voltage of 29.84 V obtained by [22], this value is slightly lower by about 0.99 V. As a different approach for determining breakdown voltages was made in [22], slightly different results are to be expected. A breakdown voltage of 28.8 V was found for the FBK LF2016 with the same method by [23]. This value agrees with the breakdown voltage determined in this thesis within the margin of error.

A calculation of the fit residuals, as described in subsection 4.1, was performed for this detector and

$$\chi^2_{\mathrm{reduced}} \approx 2.0 \tag{25}$$

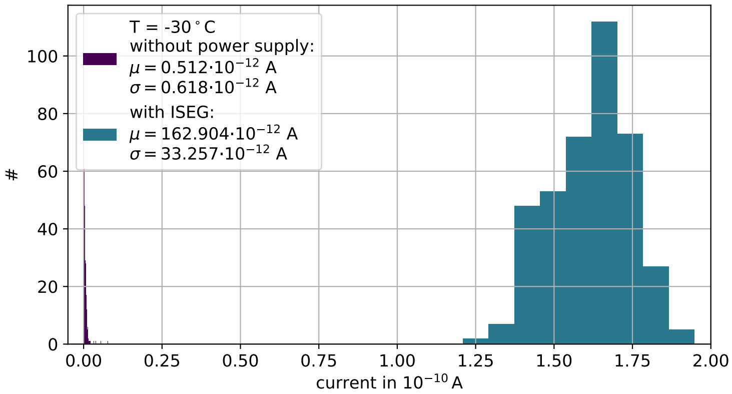

Figure 18: Histograms taken with FBK LF2016. μ and σ denote the arithmetic mean and the standard deviation of the sample. Only a small peak close to 0 A is visible for the data obtained with only the SiPM connected.

was found. This value is larger than the optimal value of 1. This indicates that the estimated errors on the breakdown voltages may be too small or that the fitted model has not enough degrees of freedom. The more probable cause in this case is the former, as the estimated errors are overall smaller than those of the other two SiPM models due to the overall higher currents and therefore better signal to noise ratio with the FBK.

Dynamic range It was also attempted to determine the dynamic range of the FBK LF2016 analogous to subsection 4.1. The temperature at which a self sustaining avalanche peak becomes visible in the differentiated data, lies at -50 °C. Therefore the dynamic range could only be determined for three temperatures. These dynamic ranges are plotted in Figure 22 and Figure 26. The uncertainties plotted with the points are estimations based on the accuracy when reading the voltages from a plot. Lower limits were determined from the plots for temperatures higher than -50 °C by measuring the voltage interval from the breakdown peak to the highest measured voltage. These limits are plotted in Figure 23 with arrows. Unlike both of the Hamamatsu devices, the dynamic range of the FBK detector drops from 8.3 V at -50 °C to 7 V at -70 °C. The lower limits for higher temperatures rise with falling temperature because the breakdown peak gets shifted to lower voltages with decreasing temperature whereas the highest measured voltage does not change its position.

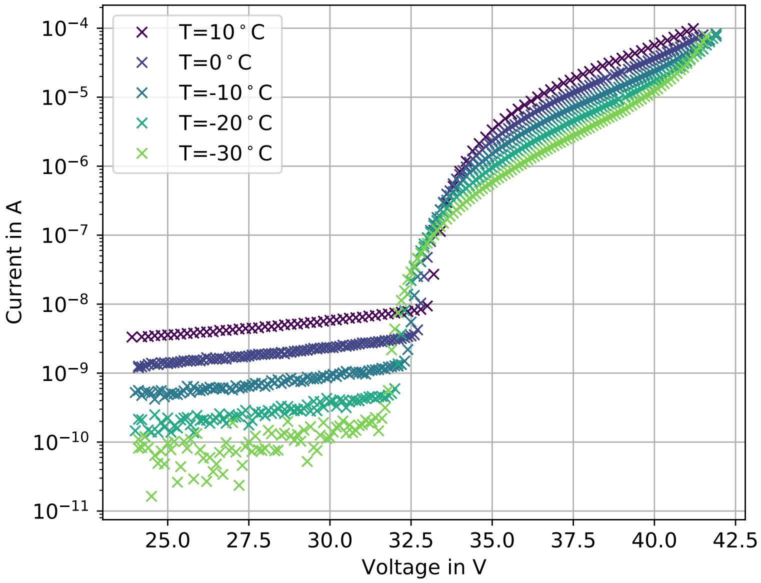

(a) Temperatures from 10 °C to -30 °C.

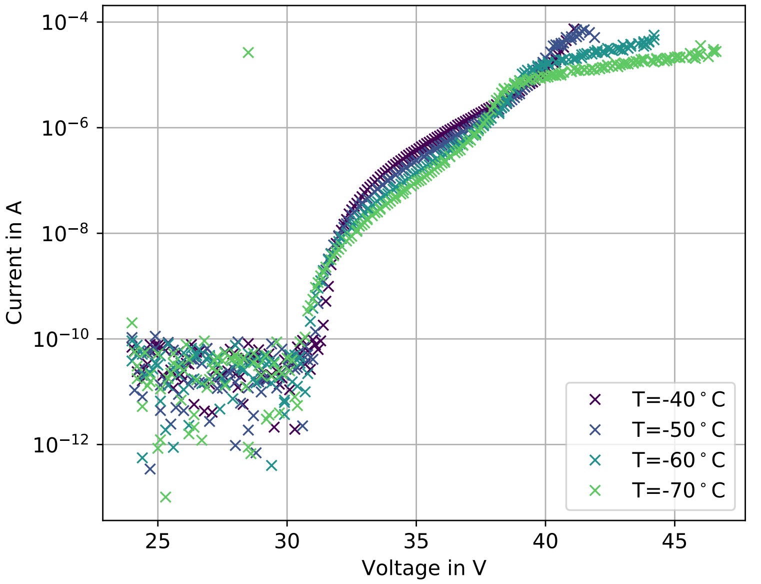

(b) Temperatures from -40 °C to -70 °C.

Figure 19: IV-Characteristics with reverse bias for FBK LF2016.

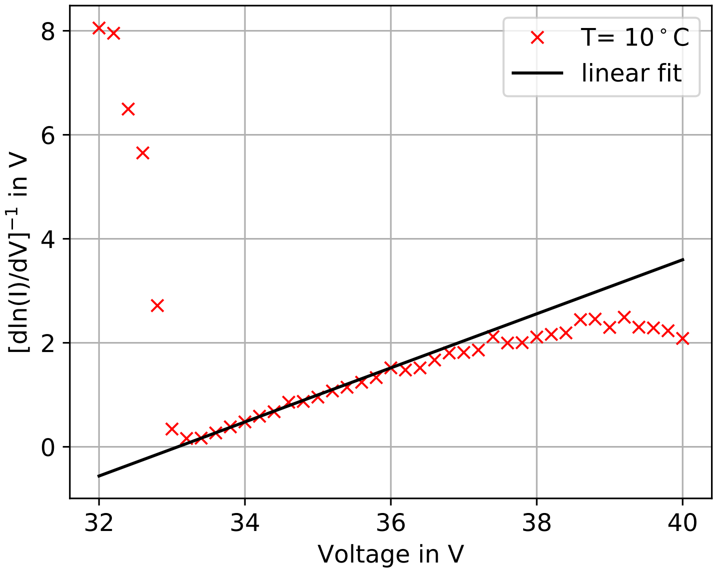

Figure 20: Example fit for determining the breakdown voltage of FBK LF2016 at 10 °C.

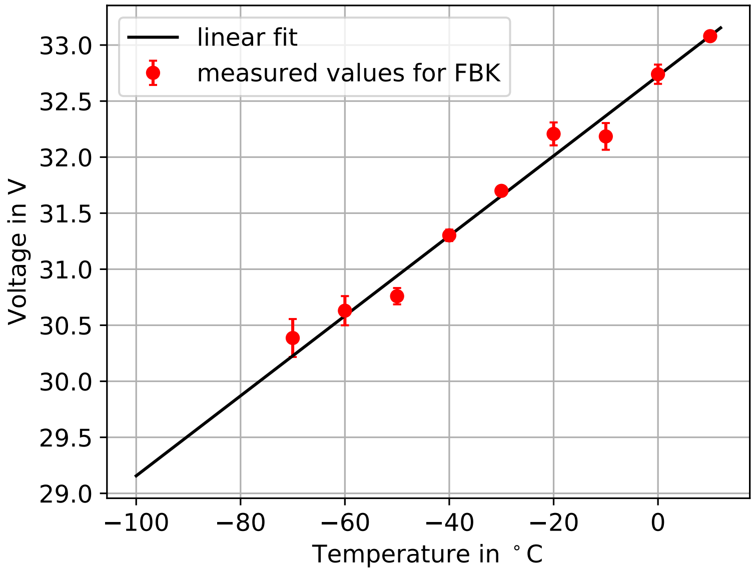

Figure 21: Plot of breakdown voltages for FBK LF2016 with linear fit for extrapolation.

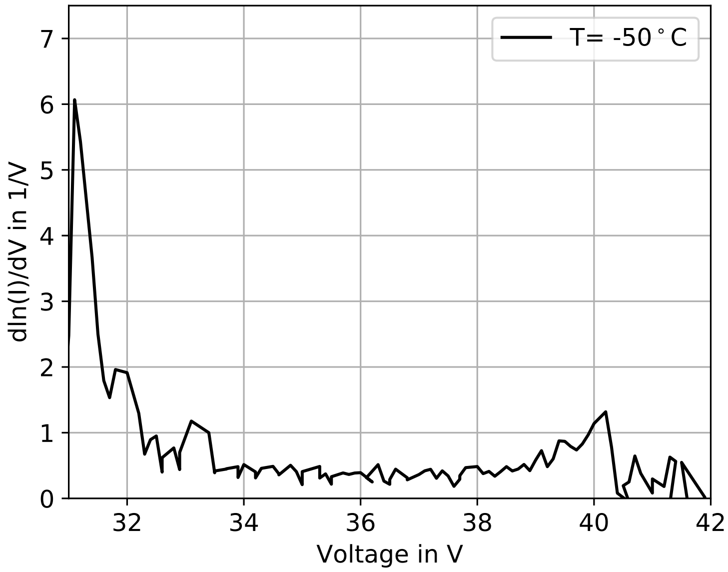

Figure 22: Derivative of logarithmic current at -50 °C for FBK LF2016.

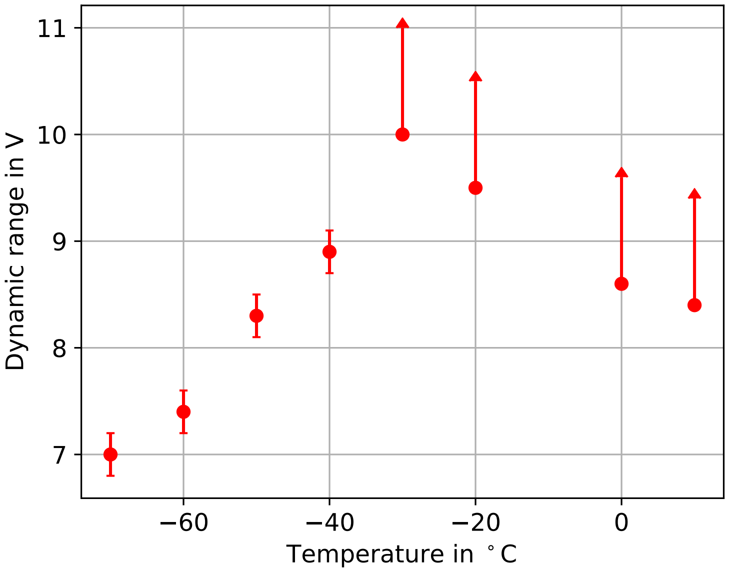

Figure 23: All dynamic ranges plotted together over their respective temperatures for FBK LF2016. Data points denoted with arrows are to be understood as lower limits.

6 Summary and Conclusion

The breakdown voltage and dynamic range for three detectors VUV3, VUV4 and FBK LF2016 was determined in this thesis. Reverse dark current characteristics were measured for temperatures down to -70°C, using a climate chamber. A drop in breakdown voltage and dark current was observed for all tested SiPM models.

A linear fit was performed at each temperature to the inverse derivative of the logarithmic data in order to determine the breakdown voltage. A second linear fit was then performed to extrapolate breakdown voltages for lower temperatures. Similar breakdown voltages and temperature dependencies were found for VUV3 and VUV4. The FBK showed a lower breakdown voltage and a weaker temperature dependence. Its extrapolated breakdown voltage at -100 °C was compared to two other results obtained by the Erlangen nEXO group using a different approach.

The dynamic range at different temperatures was read out from the plotted derivative of the logarithmic measurement data. Both Hamamatsu devices show very similar behavior as their dynamic ranges do not change with temperature. The dynamic range of the FBK drops with temperature.

Future reverse bias voltage measurements will require extensive rework to the experimental setup, as the noise limit was reached for every detector at some temperature higher than -70°C. Potential improvements can be achieved by installing proper electromagnetic shielding and using a high precision power supply. If the noise can be reduced by two orders of magnitude, even the reverse leakage current can be expected to be well above the noise limit.

7 References

[1] Zabrodskii et al.: SiPM prototype for direct VUV registration, Nuclear Instruments and Methods in Physics Research A **787**, 2015

[2] Jamil et al.: VUV-Sensitive Silicon Photomultipliers for Xenon Scintillation Light Detection in nEXO, IEEE TRANSACTIONS ON NUCLEAR SCIENCE **65**, Nov. 11, 2018

[3] Gallina et al.: Characterization of SiPM Avalanche Triggering Probabilities, IEEE Transactions on Electron Devices **66**, Oct. 10, 2019

[4] Gomez et al.: The search for neutrinoless double beta decay, Riv. Nuovo Cim **35**, 2012

[5] Schechter, J. and Valle, J.W.F: Neutrinoless double-P decay in SU(2)× U(1) theories, Physical review D **25**, June 1, 1982

[6] Kharusi et al. [nEXO Colaboration]: nEXO Pre-Conceptual Design Report, 2018

[7] Gomez et al.: Sense and sensitivity of double beta decay experiments, Journal of Cosmology and Astroparticle Physics **2011**, 2011

[8] Saveliev, Valeri: Silicon Photomultiplier - New Era of Photon Detection. In Kim Ki Young, editor, Advances in Optical and Photonic Devices, Rijeka, 2010. InTech

[9] Renker, D. and Lorenz, E.: Advances in solid state photon detectors, 2009 JINST 4 P04004

[10] Otte et al.: Characterization of Three High Efficiency and Blue Sensitive Silicon Photomultipliers, Nucl.Instrum.Meth. A846 (2017) 106-125, Jun 16, 2016

[11] Otte, N.: The Silicon Photomultiplier - A new device for High Energy Physics, Astroparticle Physics, Industrial and Medical Applications, 2006

[12] Garutti et al.: Characterization and X-Ray damage of Silicon Photomultipliers, June 2014, Procedings of Science (PoS(TIPP2014)070)

[13] KWOK K.NG: COMPLETE GUIDE TO SEMICONDUCTOR DEVICES, John Wiley & Sons, New York 2010

[14] McIntyre, Robert J.: On the Avalanche Initiation Probability of Avalanche Diodes Above the Breakdown Voltage, IEEE Transactions on Electron Devices **20**, July 1973

[15] KETEK website, accessed december 2019: `https://www.ketek.net/sipm/technology/working-principle/`

[16] ISEG website, accessed october 2019: `https://iseg-hv.com/en/products/detail/SHQ`

[17] Keithley website, accessed october 2019: `https://www.tek.com/keithley-low-level-sensitive-and-specialty-instruments`

[18] Honywell website, RTD datasheet, accessed october 2019: `https://sensing.honeywell.com/`

[19] Meilhaus website, accessed october 2019: `https://www.meilhaus.de/infos/`

[20] Testequity website, Model 1007C Temperature Chamber Specifications, accessed Novemeber 2019: `https://www.testequity.com/1007C-specs`

[21] Gallina et al.: Characterization of the Hamamatsu VUV4 MPPCs for nEXO, Nucl.Instrum.Meth. A940 (2019) 371-379, Mar 8, 2019

[22] Ziegler, Tobias: Characterisation of Silicon Photomultipliers with Xenon Scitillation Light for the nEXO Experiment, Master's Thesis, FAU Erlangen-Nürnberg, November 2016

[23] Jamil, Ako: DEVELOPMENT OF A LARGE AREA SILICON PHOTOMULTIPLIER ARRAY FOR LIGHT DETECTION IN LIQUID XENON, Master's Thesis, FAU Erlangen Nürnberg, November 2017

8 Appendix

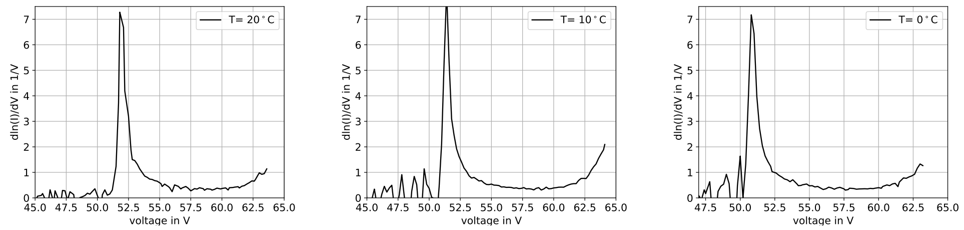

(a) 20 °C (b) 10 °C (c) 0 °C

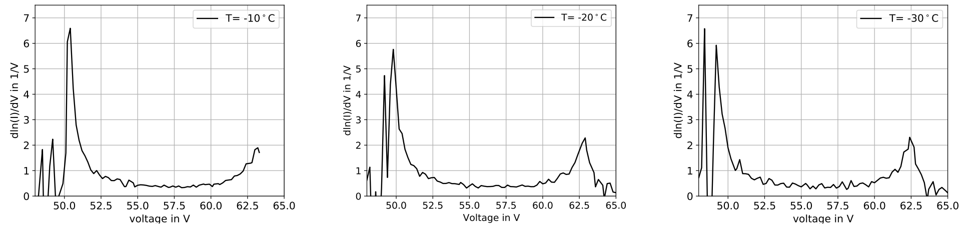

(d) -10 °C (e) -20 °C (f) -30 °C

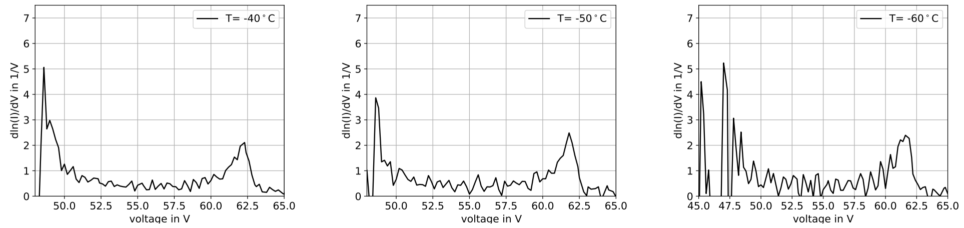

(g) -40 °C (h) -50 °C (i) -60 °C

Figure 24: Dynamic range plots of Hamamatsu VUV3 at different temperatures.

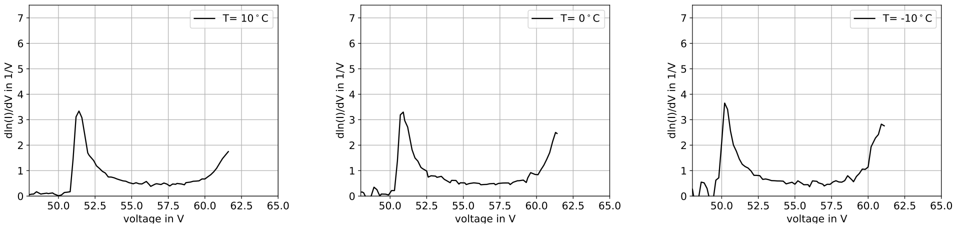

(a) 10 °C (b) 0 °C (c) -10 °C

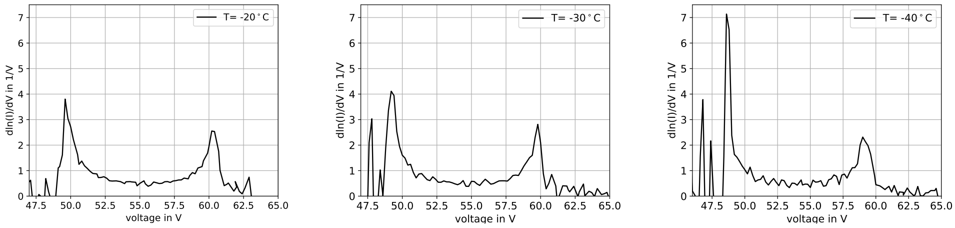

(d) -20 °C (e) -30 °C (f) -40 °C

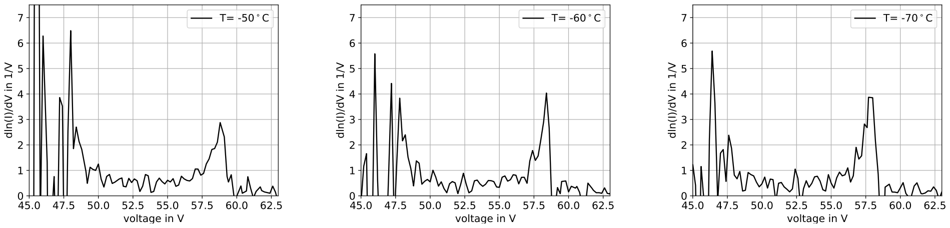

(g) -50 °C (h) -60 °C (i) -70 °C

Figure 25: Dynamic range plots of Hamamatsu VUV4 at different temperatures.

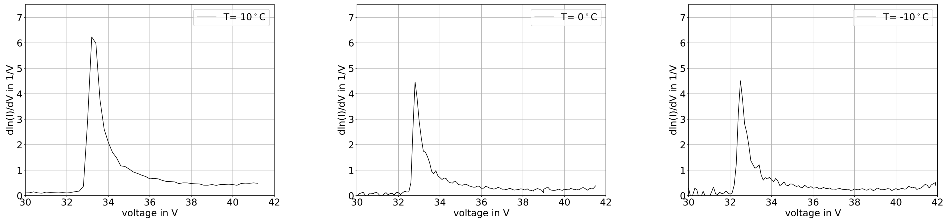

(a) 10 °C (b) 0 °C (c) -10 °C

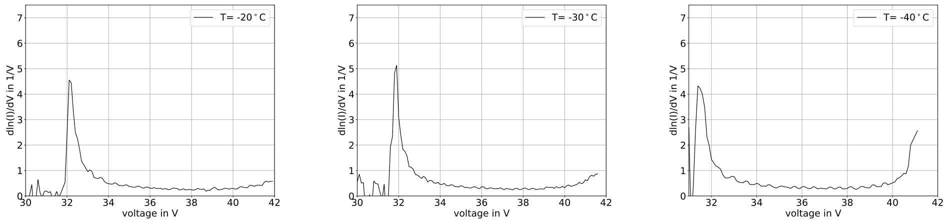

(d) -20 °C (e) -30 °C (f) -40 °C

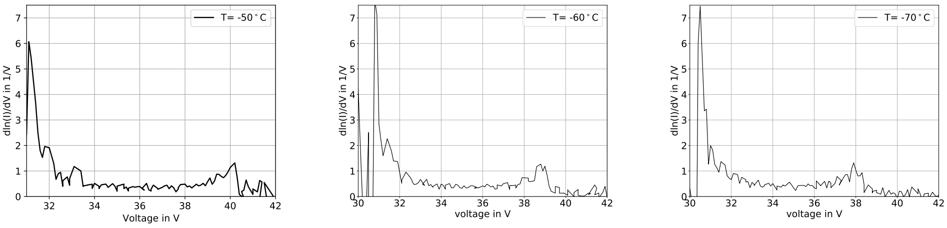

(g) -50 °C (h) -60 °C (i) -70 °C

Figure 26: Dynamic range plots of FBK LF2016 at different temperatures.

Acknowledgments

- I want to thank PD Dr. Thilo Michel for supervising me while working on this thesis.
- I also thank Michael Wagenpfeil for his support with conducting the measurements and giving valuable tips and feedback during the entire process of creating this thesis.
- My gratitude goes to the Lehmann workgroup for providing the picoammeter without which no measurements could have been conducted.
- Finally, i want to thank the entire nEXO/Medphys workgroup for interesting ideas and a lot of laughs.

Erklärung

Hiermit erkläre ich, die vorliegende Arbeit eigenständig und nur unter Verwendung der angegeben Hilfsmittel erstellt zu haben. Diese Bachelorarbeit wurde weder in gleicher noch in ähnlicher Form einer anderen Prüfungsbehörde vorgelegt.

Ort, Datum

Unterschrift